Automated Quantitative Analysis of a Mouse Model of Chronic Pulmonary Inflammation using Micro X-ray Computed Tomography

Xabier Artaechevarria[1], Daniel Pérez-Martín[1], Joseph M. Reinhardt[2], Arrate Muñoz-Barrutia[1] and Carlos Ortiz-de-Solórzano[1]

[1] Center for Applied Medical Research, University of Navarra, Pamplona, Spain
[2] Biomedical Engineering Department, University of Iowa, Iowa City, Iowa, USA

Abstract. Micro-CT has emerged as an excellent tool for in-vivo imaging of the lungs of small laboratory animals. Several studies have shown that it can be used to assess the evolution of pulmonary lung diseases in longitudinal studies. However, most of them rely on non-automatic tools for image analysis, or are merely qualitative. In this article, we present a longitudinal, quantitative study of a mouse model of silica-induced pulmonary inflammation. To automatically assess disease progression, we have devised and validated a lung segmentation method that combines threshold-based segmentation, atlas-based segmentation and level sets. Our volume measurements, based on the automatic segmentations, point at a compensation mechanism which leads to an increase of the healthy lung volume in response to the loss of functional tissue caused by inflammation.

1 Introduction

Lung cancer and chronic obstructive pulmonary disease (COPD) have high prevalence and mortality in the developed world. Recent studies point at possible common causative mechanisms between these two diseases, related to the inflammatory process triggered by external factors, mainly cigarette smoke [1, 2].

Therefore, novel experimental models are being used to study the role of inflammation in lung cancer and COPD. Among them, in vivo experiments using small animals are likely to play an important role, since they represent an essential intermediate step between the in vitro experiments and the studies on human subjects.

High resolution X-ray computed tomography (micro-CT) can be used to non-invasively discriminate tissue composition in small animals, based on the different X-ray absorption coefficients of the tissues. It is thus very well suited for imaging the lung, because the air that fills this organ provides high contrast with the surrounding tissues [3]. Giving these facts, micro-CT can be efficiently used in longitudinal experiments aimed at studying the evolution of pulmonary diseases. Namely, several previous works have shown the usefulness of micro-CT

for the study of small animal models of lung diseases, including emphysema, lung cancer, and fibrosis [4–7]. However, most of these studies rely on image analysis tools that require a great amount of user interaction or are merely qualitative.

Compared to manual or semi-automatic methods, fully automatic segmentation and quantification tools allow for accurate and reproducible measurements of disease progression. In this work, we apply these tools to a mouse model of chronic pulmonary inflammation caused by intratracheal instillation of silica. To the best of our knowledge, this is the first time that this model of inflammation is analyzed using micro-CT. Previously, Cavanaugh *et al.* had used micro-CT to quantify the extent of fibrotic and inflamed areas in a mouse model of lung injury [7]. The lung volume affected by fibrosis and inflammation was obtained by subtracting the healthy lung volume at baseline -areas of no X-ray absortion- from the healthy lung volume before the final image acquisition (a few days later). This approach assumes that the complete lung volume remains constant, which is not necessarily true. Lee *et al.* imaged the same animal model both in vivo and post mortem. The assessment was done by dividing the lung volume into 20 levels and visually assigning scores for different possible findings (honeycombing, ground-glass opacity, etc.). Generally, findings in post mortem scans correlated better with histology. Finally, Ask *et al.* studied a different fibrosis model in rats [8]. The fibrotic volumes were traced using region growing and compared to the histology-based fibrotic score.

Automatically segmenting inflammation areas in micro-CT images poses a considerable challenge. In some respects it is similar to the segmentation of computed tomography (CT) images of pathologies such as severe consolidation or extended fibrosis. Sluimer *et al.* worked on algorithms to segment scans with dense pathology [9] by combining image registration and voxel classification. More recently, Lee *et al.* used level sets to segment images of patients with diffuse interstitial lung disease (DILD) [10]. Their results were generally correct although the method failed in the most severe cases.

In this article, we propose a segmentation algorithm that combines threshold-based segmentation, atlas-based segmentation, and level sets. The method is validated by comparing computer-generated segmentations to manually-defined segmentations. The automatic segmentations of the lungs are used as masks to evaluate the extent of inflammation in a series of longitudinal scans. Quantitative measurements are performed on both diseased and healthy control mice. The rest of the article is organized as follows. In Section 2 the data acquisition method, the algorithms for lung segmentation and the disease quantification are explained. Section 3 presents the results of the segmentation evaluation, along with the disease quantification. Finally, in Section 4 some implications of the methods and results are discussed.

2 Methods

2.1 Data sets and image acquisition

We used a total of 40 A/J mice (Harlan UK Limited, Oxon, UK). The mice were 8 weeks old at the start of the experiments. Twenty-two mice were assigned to the control group and 18 to the silicosis group. Three different time points were defined for image acquisition: week 0 (before treatment), week 4, and week 14. In each group and time point, a number of animals was chosen for the follow-up study and the rest were sacrificed after the scan for purposes not relevant to this particular work. Table 1 shows the number of animals scanned in each time point.

Table 1: Animals scanned in each time point. (*) indicates that those animals were sacrificed after the scan. The rest made up the follow-up groups. Three mice of the silicosis group did not recover from the scanning protocol (one in time point 0 weeks, two in time point 4 weeks).

Time point	Control group	Silicosis group
Week 0	7 + 5*	8
Week 4	7 + 5*	7 + 5*
Week 14	7 + 5*	5 + 5*

Mice belonging to the control group were intratracheally instilled with 90 μl of saline. The silicosis group was instilled with crystalline silica (9 mg in 90 μl saline per mice). The crystalline silica sample was 99% pure alpha-quartz (Min-U-Sil 5; US Silica Co., Berkeley Springs, WV, USA), with a particle size of $< 5\ \mu m$. This single treatment causes silicosis which occurs with severe inflammation in the first weeks after instillation [11]. All procedures were carried out in compliance with European Union and University of Navarra (Institutional Animal Care and Use Committee) relevant guidelines for the use of laboratory animals.

Our imaging protocol is an adaptation of that by Namati *et al.* [12]. Animals were anesthetized with an intraperitoneal injection of 90 mg/kg ketamine and 10 mg/kg xylacine. Endotracheal intubation was performed on anesthesized animals using the BioLite system (Biotex, Houston, Texas), to illuminate the trachea with a fiber optic stylet. After intubation, animals were connected to a Flexivent rodent ventilator (Scireq, Montreal, Canada) at a rate of 200 breaths/min and a tidal volume of 10 ml/kg. Animals were kept breathing isoflurane at 2% concentration until complete relaxation was achieved and 0.5% isoflurane was maintained during the scan. 700 micro-CT projections were acquired during iso-pressure breath holds at 12 cm H_2O, which represents a physiological pressure and minimizes the probability of ventilator induced lung injury (VILI) [13]. Breath hold duration was 650 ms and normal breathing was induced during 1 s intervals between breath holds. Every 20 breath holds a total lung capac-

ity (TLC) perturbation was performed. This inflates the lung to the maximum capacity (30 cm H_2O) for 3 s and helps prevent atelectasis [14].

Images were acquired with a Micro-CAT II scanner (Siemens Pre-Clinical Solutions, Knoxville, Tennessee), with a source voltage of 80 kVp and a current of 500 μA. The exposure time per projection was 450 ms and each projection was acquired during the 650 ms iso-pressure apneae. This resulted in images of 640 slices with 1024×1024 voxels per slice, and an isotropic voxel size of 46 μm. An image of a water phantom was used as reference to convert the voxel values to Hounsfield Units (HU).

2.2 Lung segmentation

Due to the difficulty of the task, our lung segmentation algorithm combines three different segmentation strategies: threshold-based segmentation, atlas-based segmentation and geodesic active contours. This subsection details the implementation of each technique separately, concluding with the method used to combine the three segmentation results.

Threshold-based segmentation. We first segmented the healthy, i.e., low density, parts of the inflamed lungs using an algorithm largely based on previous work by Hu *et al.* [15]. Its basic steps are:

1. *Automatic thresholding*: a threshold is iteratively computed to separate air and body tissue in the scan.
2. *Background removal*: air regions connected to the borders are removed.
3. *Small volume removal*: small air volumes, which are likely to correspond to air blobs in the digestive tract, are removed.
4. *Hole filling*: possible holes within the lung are filled.
5. *Trachea extraction*: the trachea and the main airways are deleted from the volume.
6. *Small vessel inclusion*: a 3D closing operator is used to include small vessels in the lung segmentation.

With this method the largest connected area of the lung with low density is segmented, but the inflamed areas remain unsegmented.

Atlas-based segmentation. This step is essential for the correct inclusion of the diseased lung areas in the final segmentation. Furthermore, the result of this step will be used for the initialization of the final level set refinement. Atlas-based segmentation uses registration between a reference image, the atlas image, and the image to be segmented, the target image, to transform the segmentation of the atlas image into a segmentation of the target image [16].

In this case, a randomly chosen silicotic lung was manually segmented to serve as an atlas for the segmentation of the rest. Instead of directly registering the atlas and the target images, binary images containing rib segmentations were

used. The reason is that there is a large potential variability in inflammation location, extension and appearance, which can lead to errors in the registration. Although inflamed areas appear mainly near the main airways in the upper part of the lung, they can occasionally be in the lower parts too. Therefore, in all images ribs were segmented by thresholding and the resulting binary images were registered. A gaussian blurring was applied on the binarized images to help registration. The alignment process consisted of two steps: affine registration and B-Spline non-rigid registration. Mutual information was used as metric together with a stochastic gradient descent optimizer, which allows for fast and accurate registrations [17].

Geodesic Active Contours for refinement. The result of the atlas-based step is generally accurate at the ribs, has the expected lung shape in the upper, inflamed areas of the lung, but is inaccurate around the diaphragm and the heart. To refine the segmentation results in those areas we used geodesic active contours [18] . The geodesic active contours, which were implemented in ITK, follow the equation [19]:

$$\frac{d\psi}{dt} = -\alpha \mathbf{A}(\mathbf{x}) \cdot \nabla\psi - \beta P(\mathbf{x}) \cdot |\nabla\psi| + \gamma Z(\mathbf{x})\kappa \cdot |\nabla\psi| \quad (1)$$

where ψ is the level set function; α, β and γ are the weights for the advection, propagation and curvature terms, respectively; $\mathbf{A}(\mathbf{x})$ is an advection term; $P(\mathbf{x})$ is a propagation term; and $Z(\mathbf{x})$ is a spatial modifier for the curvature term κ.

To limit the refinement to the areas of interest near the diaphragm, we applied the active contour segmentation only to the lower two thirds of the lung in the coronal direction. The weights were set to 0.1 for propagation, 10 for curvature and 20 for advection. The high curvature and advection terms lead to smooth segmentations, which at the same time are strongly attracted to the edges.

Segmentation combination. The three previous segmentation results must be combined into a single final segmentation. In this fusion process, two basic assumptions are made:

- All voxels segmented by the threshold-based segmentation method or the level sets are correct.
- All voxels segmented by the atlas-based segmentation method are correct, as long as there is another lung voxel with the same x-y coordinates between the current point and the diaphragm, segmented by any of the other two methods. A x-y plane is defined as an axial or transverse slice of the micro-CT image.

With these assumptions, no extra voxel is added below the diaphragm, which is assumed to be well delineated by the combination of the threshold-based and the level sets segmentations. The atlas-based segmentation is used to add pathological areas int the upper area of the lung.

Figure 1 shows an example of the segmentation process.

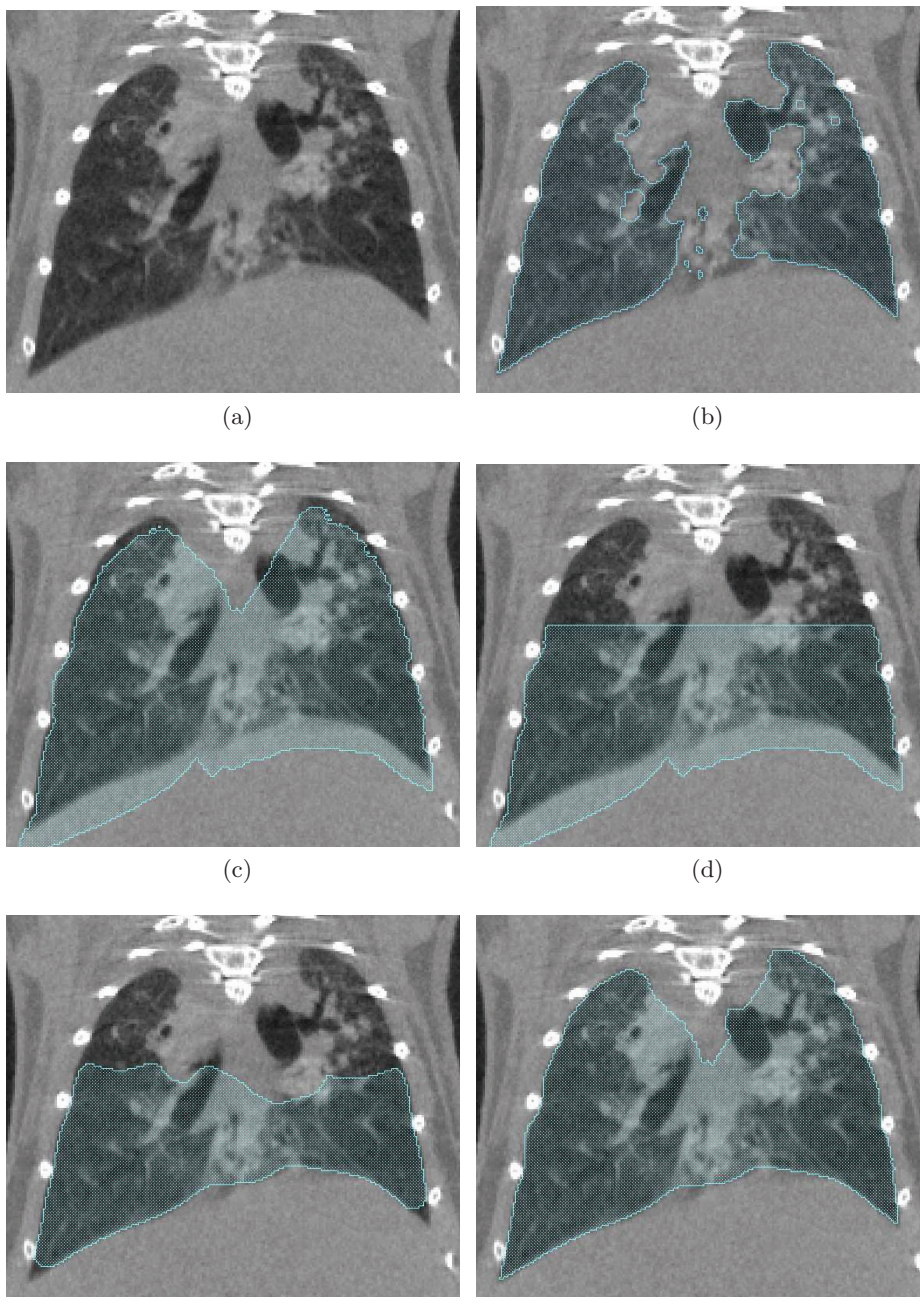

Fig. 1: (a) Micro-CT image of silicotic lung; (b) Threshold-based segmentation; (c) Atlas-based segmentation; (d) Cropped atlas-based segmentation; (e) Cropped atlas-based segmentation refined using level sets; (f) Final combined segmentation.

To segment healthy lungs, the atlas-based segmentation step was omitted. In principle, the threshold-based segmentation should suffice, but the level set method was used, with a dilated threshold-based segmentation as initial zero level set, as reported in [10]. This step was required to include the vessels in the segmentation, as occurs on the inflammation images.

In all cases an airway segmentation algorithm similar to the one reported by Artaechevarria *et al.* was used to remove the airways from the final lung segmentation [20].

3 Results

3.1 Segmentation evaluation

Six different scans were manually traced using the Amira software (Visage Imaging, Fürth, Germany) and were used as reference for the evaluation of the automatic segmentation method. The similarity index (SI) between the manual and the automatic segmentations was computed. The SI between two segmentations, S_a and S_b, of the same object, is defined as:

$$SI = \frac{2|S_a \bigcap S_b|}{|S_a| + |S_b|}, \tag{2}$$

where $\bigcap$ indicates the overlapping voxels between the two segmentations, and $|S_a|$ indicates the number of voxels of the corresponding segmentation [21]. SI has value 1 when there is a perfect match between labels and 0 when there is no overlap.

Table 2 shows the SI for the six manually segmented images. The average SI is 0.95.

Table 2: SI for the six manually segmented images

Image number and group	Similarity Index
Image 1 (control, week 0)	0.97
Image 2 (silica, week 0)	0.97
Image 3 (silica, week 4)	0.94
Image 4 (silica, week 4)	0.96
Image 5 (silica, week 14)	0.94
Image 6 (silica, week 14)	0.93

3.2 Disease quantification

Four different measurements were performed on the segmented lungs, in order to assess the effect of the inflammation:

1. *Total Lung Volume (TLV)*: corresponds to the final segmentation.
2. *Healthy Lung Volume (HLV)*: the result of the threshold-based segmentation.
3. *Inflamed Lung Volume (ILV)*: computed as TLV−HLV.
4. *Mean Lung Intensity (MLI)*: in HU, considering the complete lung.

Figure 2 shows the mean values of these parameters in control and diseased mice. There are no statistically significant differences between groups before treatment, but in weeks 4 and 14 silicotic mice show higher MLI, ILV and TLV. HLV is larger in the silica group only at week 4.

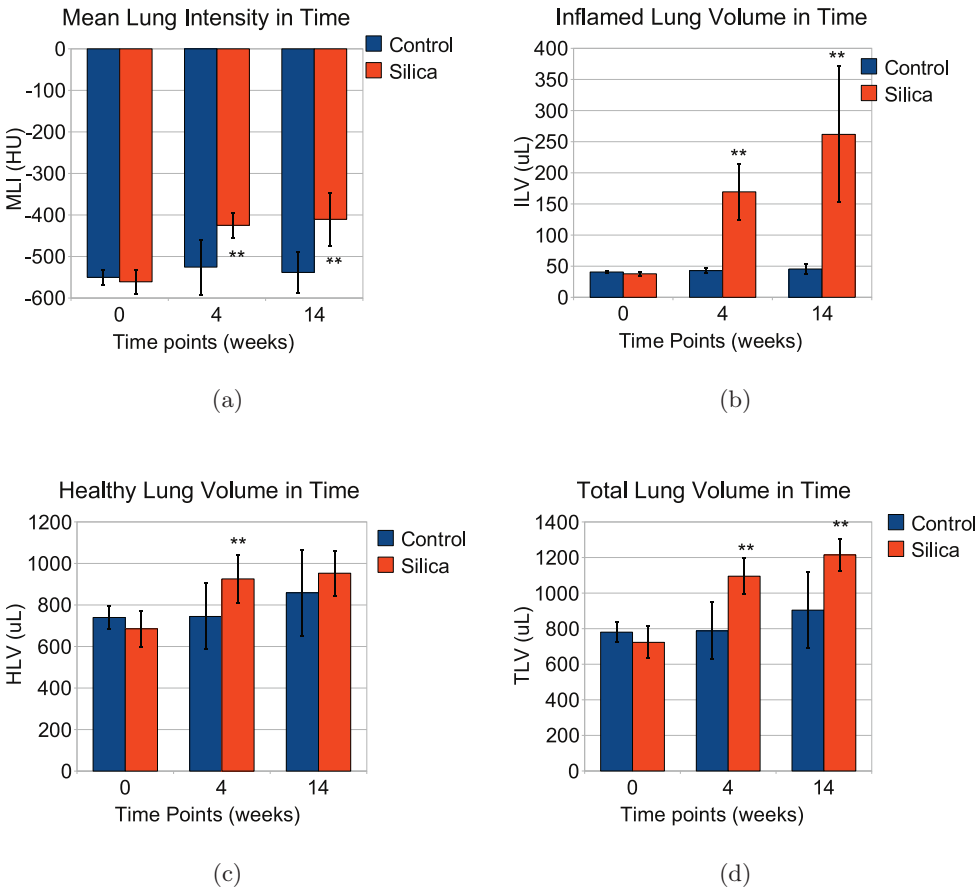

Fig. 2: (a) MLI vs. time points; (b) ILV vs. time points; (c) HLV vs. time points; (d) TLV vs. time points. (**) indicates $p < 0.05$, according to the MannWhitney U test. Error bars reflect the standard deviation within the group.

4 Discussion

The quantitative study of this model of lung disease using micro-CT requires accurate segmentations of the lungs. Automatic segmentation methods such as the one described in this work are essential, because manual segmentations are very time consuming, requiring as much as 5 hours in the diseased cases. Even though further evaluation is required, preliminary results show that our automatic segmentation method yields accurate results.

Atlas-based segmentation is one of the steps of the automatic segmentation method. A randomly chosen image of the silicosis group was chosen as the atlas image. Segmentation accuracy results show that this approach does not lead to large errors, but overall accuracy could improve with the use of a more generic atlas.

The calculated quantitative values are highly informative. As expected, we found a statistically significant increase of ILV and MLI in diseased versus to control animals. However, the higher HLV and TLV values found in silicotic mice compared to control ones requires further analysis. This result suggests that a compensatory mechanism exists, through which the healthy lung volume increases in response to the loss of functional tissue caused by inflammation. Further study, including histology and pulmonary functional tests, will be required to gain more knowledge on this phenomenon. It is also noteworthy that the mean ILV grows considerably within the diseased mice from week 4 to week 14, although a large variability exists.

In conclusion, we have shown that automatic image segmentation and quantification on a mouse model of lung inflammation can point at relevant biological issues. The intrinsic complexity of the segmentation task has produced the need for a custom segmentation method, within which several well-known methods are combined taking the characteristics of the expected disease into account.

References

1. de Torres, J.P., Bastarrika, G., Wisnivesky, J.P., Alcaide, A.B., Campo, A., Seijo, L.M., Pueyo, J.C., Villanueva, A., Lozano, M.D., Montes, U., Montuenga, L., Zulueta, J.J.: Assessing the Relationship Between Lung Cancer Risk and Emphysema Detected on Low-Dose CT of the Chest. Chest **132**(6) (2007) 1932–1938
2. Houghton, A.M., Mouded, M., Shapiro, S.D.: Common origins of lung cancer and COPD. Nature Medicine **14**(10) (2008) 1023–1024
3. Johnson, K.A.: Imaging Techniques for Small Animal Imaging Models of Pulmonary Disease: Micro-CT. Toxicologic Pathology **35**(1) (2007) 59–64
4. Recheis, W., McLennan, G., Ross, A.F., Hoffman, E.A.: Imaging the mouse lung with micro-CT. In: Molecular Imaging of the Lungs. Taylor and Francis (2005)
5. Froese, A.R., Ask, K., Labiris, R., Farncombe, T., Warburton, D., Inman, M.D., Gauldie, J., Kolb, M.: Three-dimensional computed tomography imaging in an animal model of emphysema. European Respiratory Journal **30**(6) (2007) 1082–1089

6. De Clerck, N., Meurrens, K., Weiler, H., Dyck, D.V., Greet, G.V., Terpstra, P., Postnov, A.: High-resolution X-ray microtomography for the detection of lung tumors in living mice. Neoplasia **6**(4) (2004) 374–379
7. Cavanaugh, D., Travis, E.L., Price, R.E., Gladish, G., White, R.A., Wang, M., Cody, D.D.: Quantification of bleomycin-induced murine lung damage in vivo with micro-computed tomography. Academic Radiology **13**(12) (2006) 1505 – 1512
8. Ask, K., Labiris, R., Farkas, L., Moeller, A., Froese, A., Farncombe, T., McClelland, G.B., Inman, M., Gauldie1, J., Kolb, M.R.: Comparison between conventional and "clinical" assessment of experimental lung fibrosis. Journal of Translational Medicine **6**(16) (2008)
9. Sluimer, I., Prokop, M., van Ginneken, B.: Toward automated segmentation of the pathological lung in CT. IEEE Transactions on Medical Imaging **24**(8) (2005) 1025– 1038
10. Lee, J., Seo, J.B., Kim, N., Park, S.O., Lee, H., Shin, Y.G., Kim, S.H.: Novel level-set based segmentation method of the lung at HRCT images of diffuse interstitial lung disease (DILD). In: SPIE Medical Imaging 2009: Image Processing. Volume 7259.
11. Saffiotti, U., Williams, A., Daniel, L., Kaighn, M., Mao, Y., Shi, X.: Carcinogenesis by crystalline silica: Animal, cellular, and molecular studies. In: Silica and silica-induced lung diseases. CRC Press (1996)
12. Namati, E., Chon, D., Thiesse, J., Hoffman, E.A., de Ryk, J., Ross, A., McLennan, G.: In vivo micro-CT lung imaging via a computer-controlled intermittent iso-pressure breath hold (IIBH) technique. Physics in Medicine and Biology **51**(23) (2006) 6061–6075
13. Dreyfuss, D., Saumon, G.: Ventilator-induced Lung Injury . Lessons from Experimental Studies. American Journal of Respiratory and Critical Care Medicine **157**(1) (1998) 294–323
14. Allen, G.B., Suratt, B.T., Rinaldi, L., Petty, J.M., Bates, J.H.T.: Choosing the frequency of deep inflation in mice: balancing recruitment against ventilator-induced lung injury. American Journal of Physiology - Lung Cellular and Molecular Physiology **291**(4) (2006) 710–717
15. Hu, S., Hoffman, E., Reinhardt, J.: Automatic lung segmentation for accurate quantitation of volumetric X-ray CT images. IEEE Transactions on Medical Imaging **20**(6) (2001) 490–498
16. Rohlfing, T., Brandt, R., Menzel, R., Russakoff, D.B., Maurer, Jr., C.R.: Quo vadis, atlas-based segmentation? In: The Handbook of Medical Image Analysis – Volume III: Registration Models. Kluwer Academic / Plenum Publishers (2005) 435–486
17. Klein, S., Staring, M., Pluim, J.: Evaluation of Optimization Methods for Non-rigid Medical Image Registration using Mutual Information and B-splines. IEEE Transactions on Image Processing **16**(12) (December 2007) 2879–2890
18. Caselles, V., Kimmel, R., Sapiro, G.: Geodesic active contours. International Journal of Computer Vision **22** (1995) 61–79
19. Ibanez, L., Schroeder, W., Ng, L., Cates, J.: ITK Software Guide. Kitware (2005)
20. Artaechevarria, X., Muñoz-Barrutia, A., van Ginneken, B., Ortiz-de-Solórzano, C.: Fast murine airway segmentation and reconstruction in micro-CT images. In: SPIE Medical Imaging 2009: Biomedical Applications in Molecular, Structural, and Functional Imaging. Volume 7262.
21. Zijdenbos, A., Dawant, B., Margolin, R., Palmer, A.: Morphometric analysis of white matter lesions in MR images: Method and validation. IEEE Transactions on Medical Imaging **13**(4) (Dec 1994) 716–724